Synthesis of Manganese Nitride Doped with Rare-Earth Elements and Their Oxygen Reduction Reaction Activity

Hayato Sakai[1], Shigeto Hirai[2], Masanori Nagao[3], Nataly Carolina Rosero-Navarro[4,5], Akira Miura[4]*, Kiyoharu Tadanaga[4]

[1] Graduate School of Chemical Sciences and Engineering, Hokkaido University, N13W8 Sapporo 060-8628, Japan

[2] School of Earth, Energy and Environmental Engineering, Kitami Institute of Technology, 165 Koen-cho, Kitami 090-8507, Japan.

[3] University of Yamanashi, 7-32 Miyamae, Kofu, Yamanashi 400-0021, Japan.

[4] Faculty of Engineering, Hokkaido University, N13W8 Sapporo 060-8628, Japan.

[5] Instituto de Cerámica y Vidrio (CSIC), Campus de Cantoblanco, 28049, Madrid, Spain.

* Corresponding author: e-mail amiura@eng.hokudai.ac.jp

Keywords: nitride materials, electrode materials, fuel cells, catalysis, electrochemical reactions

Abstract

Binary and ternary metal nitrides with d-block elements have been attracting attention as non-platinum oxygen reduction reaction (ORR) electrocatalysts. However, nitrides with f-block elements have not been explored as ORR catalysts, presumably because of their instability in an aqueous solution. By combining the stability of d-block metal nitrides in an alkaline solution and a high affinity toward OH^- of the f-block elements, novel ORR nitride catalysts in an aqueous alkaline solution would emerge. Herein, we synthesized novel manganese nitrides with rare-earth elements (Y, Er, Tm, Yb) via the self-combustion reaction and evaluated their ORR activities in an aqueous alkaline solution. Ytterbium-doped manganese nitrides with different compositions were synthesized by the combustion reactions between $MnCl_2$-$YbCl_3$ mixtures and $NaNH_2$ powder. The lattice parameter of the synthesized nitrides increased with an increase in the concentration of rare-earth elements, and EDX exhibited the distribution of Mn and Yb on the nanometer scale. A significant change in the magnetic properties by adding Yb supported the incorporation of Yb into an MnN framework. The enhancement of the ORR activity and high affinity of OH^- on the surface were found in the nitride catalysts with ~1% Yb/Mn ratio. In addition, manganese nitrides containing small amounts of various rare-earth elements (Y, Er, Gd, Tm) with enhanced catalytic activities were also synthesized. This work provides new strategies for synthesizing metal nitrides with rare-earth elements, and for improving the ORR catalytic activities of metal nitrides by doping rare-earth elements.

Introduction

Highly efficient energy-conversion devices are the key to carbon neutrality, which is considered to be the urgent mission for sustainable energy[1–3]. Fuel cells are energy conversion devices, converting the chemical energy of hydrogen and oxygen gases into electric energy[4,5]. However, the large overpotential of the cathode reaction, i.e., the oxygen reduction reaction (ORR), limits their energy conversion efficiency[6,7]. Pt catalysts are the most active electrochemical catalysts for ORR[7–9], but their cost and limited abundance hinder their use. Accordingly, binary platinum alloys/intermetallics have been studied as a way to decrease the usage of Pt and enhance catalytic activity[10–16].

Metal nitrides have attracted attention as non-platinum catalysts because of their electrical conductivity and chemical stability[17–26]. For instance, binary transition metal nitrides such as MnN_x[19–21], Fe_3N[19], Co_3N[19,22,23], Ni_3N[19,24], ZrN[25], and MoN_x[26] have been studied as ORR catalysts that do not use noble metals. Like Pt-based catalysts, Doping elements into binary nitrides show higher activity than the host nitrides[27–31]; Co doping for VN ($V_{0.95}Co_{0.05}N$[30]) and Mn doping for Mo_2N ($Mn_{0.12}Mo_{0.88}N_{0.5}$[31]) improve the ORR activity. Despite these attractive aspects, most of the exploration of highly effective catalysts has been limited to nitrides containing d-block metals. To our knowledge, ternary nitrides composed of both d-block and f-block elements are limited, such as Ce_2MnN_3[32], $LaWN_3$[33], $LnReN_3$[34], and these have not been examined as catalysts in an aqueous solution.

f-block oxides have a high affinity for hydroxide ions[35], which can affect the formation and dissociation of hydroxyl groups in the ORR process in an alkaline aqueous solution. This motivated us to explore ternary nitride catalysts containing 4f-block metals. The rate-determining step process of this ORR mechanism is understood by either displacement or regeneration of the OH^- surface in the metal hydroxides[36,37]. Metal nitrides form thin oxide or hydroxide layers on

the surface in the air[19,24,25], which are considered to act as the active sites for ORR. Therefore, we postulated that the inclusion of f-block elements in the metal nitrides would improve the ORR activity by increasing the affinity of the OH^- on their surface.

In this study, we synthesized new manganese nitrides with doped with rare-earth elements for the ORR electrocatalysts in an alkaline aqueous solution. Manganese nitrides were selected as host materials of the ORR catalyst[19–21]. The nitride catalysts were synthesized via combustion reactions from $MnCl_2$, RCl_3 (R = Y, Gd, Er, Tm, Yb), and $NaNH_2$. Their ORR activities in alkaline solutions were enhanced by incorporating only ~1% rare-earth elements regardless of the rare-earth species.

1. Experimental

1.1 Synthesis of Nitrides

Manganese nitrides were synthesized using the self-combustion reaction as previously reported[38–41]. Since metal chloride and $NaNH_2$ powder are sensitive to moisture, these powders were handled in a glove box with an Ar atmosphere. A Teflon-lined autoclave with an inner volume of 70 mL (Yanako, AD-70) was heated at 493 K overnight to remove any water before the synthesis reaction. $MnCl_2$, $YbCl_3$, and $NaNH_2$ powders with a molar ratio of 1: y (y=0, 0.05, 0.1, 0.2):10 were mixed for about 20 minutes using an agate mortar. This mixture and a magnetic stirrer were added to a tightly closed autoclave. Magnetic stirring was conducted for 1 min to mix the powders in the closed autoclave. The reaction was then initiated by heating the mixture at 493 K and keeping it there for 18 hours. *Caution! When these powders are mixed and heated, a violent exothermic reaction occurs. Synthesis using large amounts of starting material can cause serious accidents. The total mass of these powders was less than 700 mg.*

Under the ambient atmosphere, the resulting products were washed with ethanol and water to remove the NaCl byproduct and unreacted starting materials. The final product was collected after three centrifuges with distilled water. The same process was employed for synthesizing the nitrides doped with Y, Gd, Er, Tm by using RCl_3 (R = Y, Gd, Er, Tm) as a raw material.

The crystal structure was investigated by XRD with Cu Kα radiation (Rigaku, Miniflex600). The morphology and elemental distribution were observed using SEM-EDX (Hitachi, TM3030 Plus) and STEM-EDX (Hitachi, HD-2000). The elemental composition was quantified using ICP-OES (Shimadzu, ICPE-9000). The surfaces of the powders were examined by XPS (JEOL, JPS-9200). The binding energies were corrected by reference to free carbon (284.6 eV). The Mn K-edge XANES spectra were measured in transmission mode at the BL5S1 beamline of the Aichi Synchrotron with the approval numbers 2021D2001 and 202104005. The magnetic properties

were measured using a vibrating sample magnetometer and a physical property measurement system (PPMSDynaCool).

1.2 ORR Measurements

The ORR catalytic activities were measured using a three-electrode cell with a rotating disk electrode system (RRDE-3A) in an oxygen-saturated 1 M KOH aqueous solution. The cell consisted of a glassy carbon working electrode, a Pt-wire counter electrode, and an Hg/HgO reference electrode. Catalyst-loaded electrodes were prepared by four-times-pipetting and drying 2 μL of the catalyst ink. The ink was prepared via ultrasonication of a mixture of nitride (2 mg), Vulcan carbon (2 mg), and ionomer (Tokuyama Corporation, 60 μL) in ethanol (540 μL).

The discontinuous gap of the current value of ~0.15 mA cm^{-2} due to the automatic switching of the current range of the potentiostat was manually connected by connecting the points of 0.15 mA cm^{-2} and 0.20 mA cm^{-2} with a straight line.

2. Results

2.1 Synthesis and Evaluation of Yb-Doped Manganese Nitrides

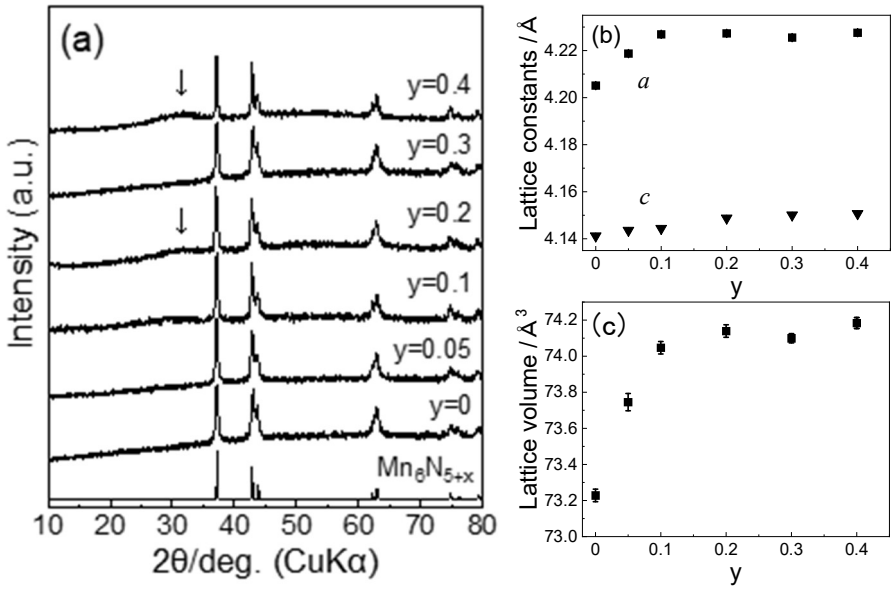

Fig. 1. (a) XRD patterns of non-doped manganese nitride and Yb-doped manganese nitrides. ↓ shows halo patterns. (b) Lattice constants, *a* and *c*, of tetragonal manganese nitrides. (c) Lattice volumes of tetragonal manganese nitrides.

Table 1. Quantitative ratio of Yb/Mn for the synthesized nitrides acquired by ICP and EDX. By EDX measurements, eight points were measured for each sample.

y (Yb/Mn)	ICP	EDX
0	0	0
0.05	0.016	0.0070(16)*
0.1	0.101	0.098(9)
0.2	0.223	0.226(12)
0.3	0.495	0.45(17)
0.4	0.803	0.68(15)

*The Yb signal was detected.

Fig. 1(a) shows the XRD patterns of the nitrides synthesized from the starting materials with a different molar ratio of $YbCl_3/MnCl_2$, which is noted as y. The diffraction peaks are indexed as the tetragonal rock-salt structure, which is reported as Mn_6N_{5+x}[42]. Fig. 1(b-c) show the lattice constants and volumes. While the lattice constant, *a*, increased up to y=0.1 and did not change above 0.1, the lattice constant, *c*, increased slightly up to y=0.2. As a result, the lattice volume increases up to y=0.2. Therefore, the solubility limit would be y=0.2 or below. A further increase showed a halo pattern at approximately 30°, suggesting the formation of an amorphous phase (Fig. S1). Minor amorphous halo is shown with y=0.2 and becomes strong with y=0.4, but little is detected in y=0.3. Although this intensity does not increase linearly, this supports the solubility limit of 0.2 or below. The molar ratio of Yb / Mn was determined by EDX, which increased with increasing Yb content (Table 1). The Yb / Mn ratio determined by ICP was 0.016 when y = 0.05 and 0.101 when y = 0.1, which was comparable to the EDX results. When y = 0.3 or higher, the EDX results showed a larger amount of Yb compared with the starting composition (y). The

washing in water after the synthesis should decompose YbN, presumably form Yb-O-H amorphous. Because there was a halo pattern at higher Yb content, this may be due to the formation of amorphous $Yb(OH)_3 \cdot xH_2O$ or $Yb_2O_3 \cdot xH_2O$ (Figs. S2 and 3). The solubility of $Mn(OH)_2$ (3.39×10^{-5} mol/L[43]) is significantly higher than that of $Yb(OH)_3$ (9.60×10^{-8} mol/L[35]). Therefore, more manganese can dissolve in a highly concentrated NaOH aqueous solution that forms during washing with water, and ytterbium hydroxides can precipitate.

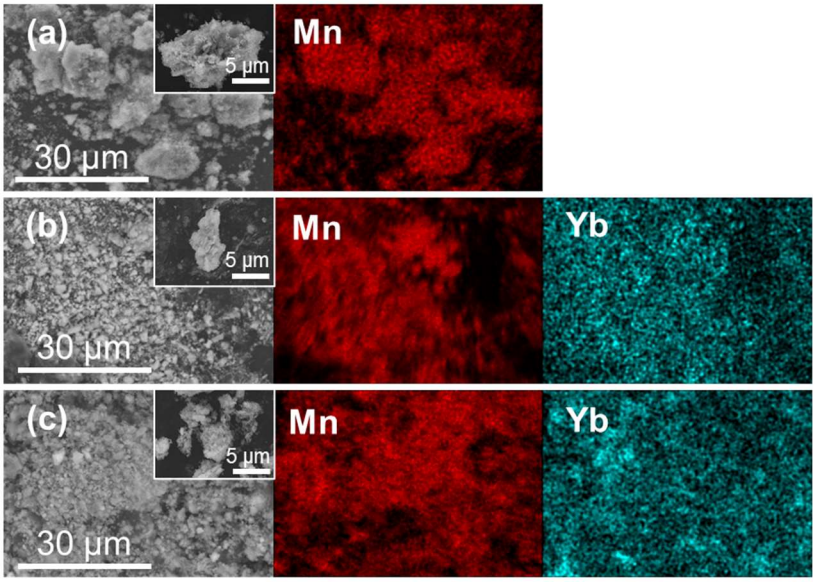

Fig. 2. SEM-EDX images of (a) y=0, (b) y=0.05, and (c) y=0.1 samples.

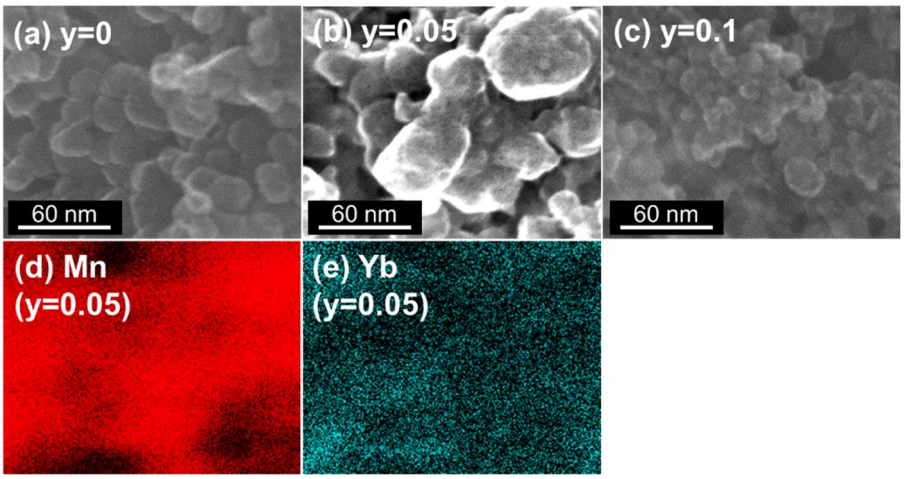

Fig. 3. STEM images of (a) y=0, (b) y=0.05, and (c) y=0.1 samples, and EDX elemental maps of y=0.05 (d-e) sample.

The morphology and distribution of the elements were characterized by SEM-EDX (Fig. 2) and STEM-EDX (Fig. 3). The SEM images showed aggregated micron-sized particles as the products. The size of aggregated particle size is approximately 3-15 um. The Yb signal was detected for the products synthesized from $YbCl_3$ in addition to Mn and N signals. As shown in Fig. 3, Yb and Mn were distributed in the same area in the micron scale even though Yb was segregated in some regions in the cases of y=0.1 and 0.2. The STEM images showed micron-sized aggregates composed of nanoparticles in the size of a few to several tens of nanometers. STEM-EDX showed the distribution of Yb in the nanoscale (Fig. 3). The particle size of y = 0.05 was several times larger than that of y=0 and y=0.1. EDX mapping of y=0.05 did not detect the segregated region of Yb.

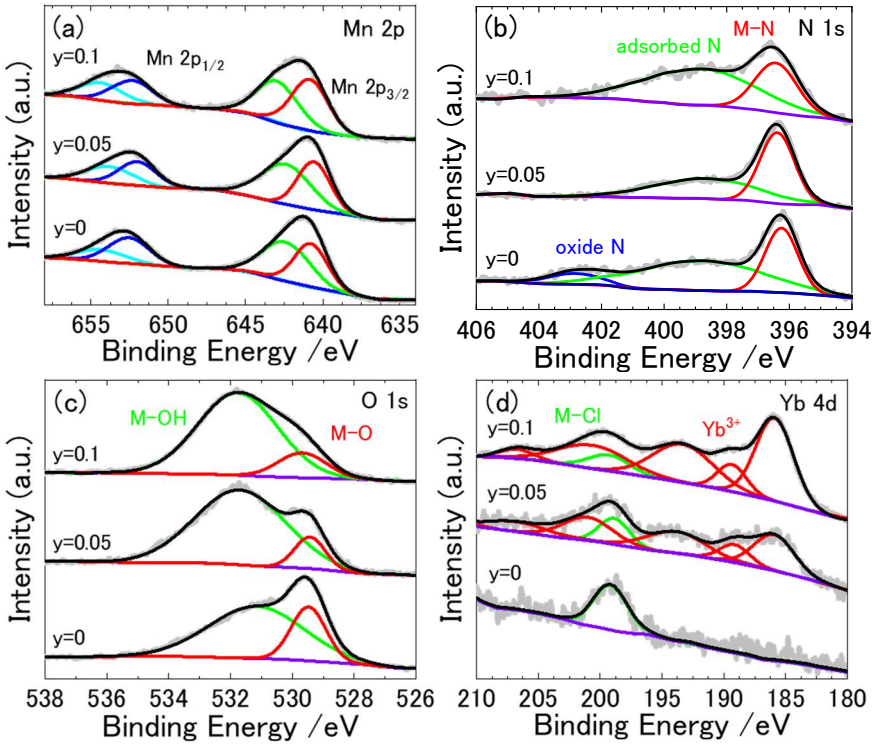

Fig. 4. XPS spectra in the (a) Mn 2p, (b) N 1s, (c) O 1s, and (d) Yb 4d regions for y=0, 0.05,

and 0.1 samples.

The electronic structures of the surface and bulk were evaluated using X-ray photoelectron spectroscopy (XPS) and X-ray absorption, respectively. Fig. 4 shows the XPS spectra of the products with different Yb amounts. As shown in Fig. 4(a), the Mn $2p_{1/2}$ and $2p_{3/2}$ peaks were found in three samples, and their splitting widths were about 11.0 eV[44,45]. The N 1s spectrum in Fig. 4(b) shows a peak attributed to metal nitrides (about 396 eV) and a faint oxidation tail in the high energy range[46]. As the concentration of Yb increased, the M-N peak intensity became smaller. Fig. 4(c) shows the O 1s spectrum of the products. A peak attributed to metal oxides at about 529 eV and a peak attributed to metal hydroxides at about 532 eV were observed in the three samples[47]. In the non-doped sample, the oxide peak was the main one, whereas in the Yb-doped sample, the hydroxide peak became larger as the Yb fraction increased. Table S1 shows XPS O 1s data including peak positions and area. Doping of Yb (y=0.05) increased the area of OH^- from 67.0 % to 82.3%, and that of Yb (y=0.10) further increased to 87.9 %. Yb had a high affinity toward hydroxide ions[35], which can play an important role in the ORR process. The peaks of Yb^{3+} (Fig. 4(d)) are known to be very complex, but the two main peaks can be assigned to the peaks attributed to the $^3H_6$ and $^1G_4$ terms (185.0 eV) and the $^3G_6$ and $^1F_3$ terms (192.5 eV), respectively[48]. The peak at about 199 eV is attributed to metal chlorides, which may be attributed to a small amount of residual raw material chlorides or NaCl[49,50].

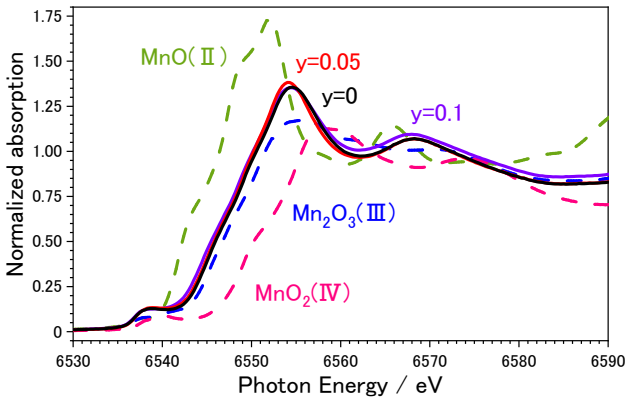

Fig. 5. Mn K-edge XANES spectra of y=0, 0.05, and y=0.1 samples. The broken lines are the spectra of the reference samples.

Fig. 5 shows the Mn K-edge XANES spectra of the y=0, y=0.05, and y=0.1 samples. Both the y=0 and y=0.05 samples showed a similar absorption spectrum, indicating that the valence of Mn was not changed by Yb incorporation. The energy of the absorption edge was close to that of trivalent Mn_2O_3, indicating that the valence was close to three. The energy in the absorption edge of the synthesized nitrides lower than that of Mn_2O_3 can be attributed to the nonstoichiometric feature of Mn_6N_{5+x}.

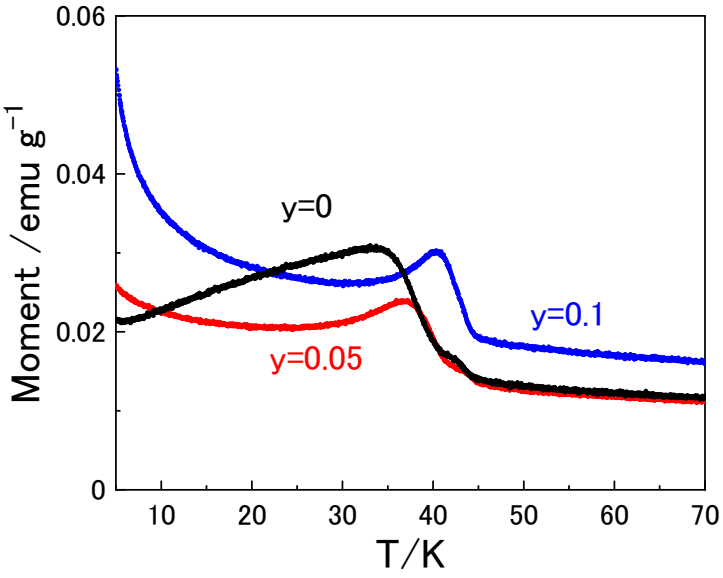

Fig. 6. Temperature dependence of the zero-field-cooled (ZFC) magnetization plots of the y=0, 0.05, and 0.1 Mn-Yb-N samples. The magnetic field is 250 *Oe*.

To confirm the effect of the addition of rare earth to manganese nitrides on magnetic properties, the temperature dependence of the magnetic properties was examined (Fig.6). The magnetic moment rise below ~20 K in Yb-doped manganese nitride is attributed to the emergence of the magnetic moment of the Yb^{3+} ions[51]. A hump in the magnetic moment of manganese nitrides (y=0) was seen at 35 K. An increase in Yb content increased this temperature to 38 K at y=0.05 and to 41 K at y=0.1. The change in the magnetic moment at 30-40 K can be attributed to the change in the magnetic property of Yb-doping in manganese nitrides. In the literature, the $Mn_6N_{5.26}$ is reported to show antiferromagnetic structure at room temperature, and the magnetic moment dependence between 323-673 K shows that its Néel point is at 660 K[42]. Thus, the origin of the change in the magnetic moment at low temperatures may be attributed to another magnetic transition of manganese nitrides, but the possibility of impurity phases needs to be investigated. In order to exclude the possibility of magnetic transition of Yb-O-H, we also measured the magnetic properties of the amorphous Yb-O-H precipitate synthesized by mixing $YbCl_3$ and NaOH in an aqueous solution. This did not show such a hump near 40 K, suggesting that the amorphous Yb-O-H precipitate is not the origin of this magnetic change (Fig. S4).

2.2 ORR Measurement of Yb-doped Manganese Nitrides

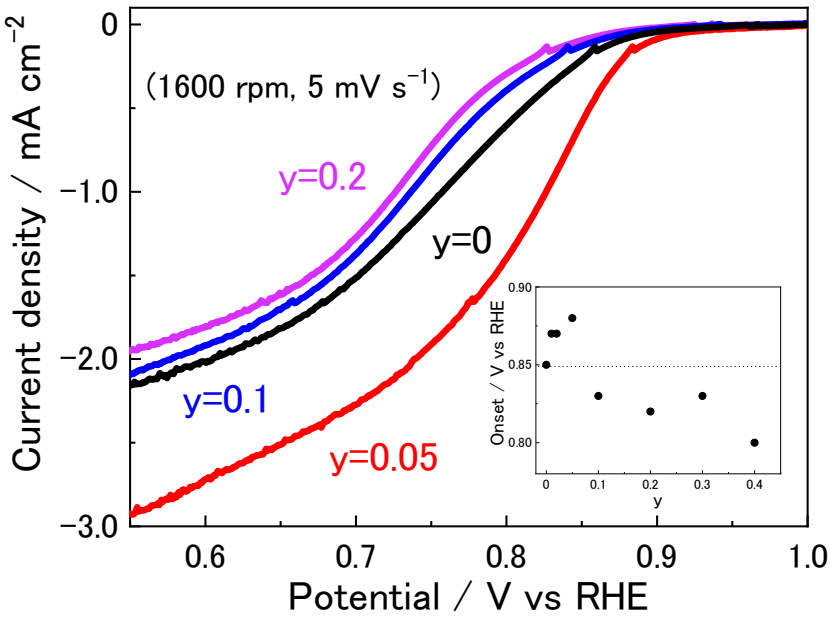

Fig. 7. LSV polarization curves of the y=0, 0.05, 0.1, and 0.2 Mn-Yb-N samples. The inserted figure shows ORR onset potential vs y. The onset potential was defined as the potential when the current density reached -0.2 mA cm^{-2}.

The catalytic activity of Yb-doped manganese nitrides for ORR was evaluated using linear sweep voltammetry (LSV) with RDE. Fig. 7 shows the LSV results of the products. The y=0.05 sample showed the highest onset potential for ORR, and gradually lower onset potentials were observed with an increase in the percentage of Yb in the manganese nitride.

The insert figure shows the ORR onset potential vs. the Yb/Mn ratio (=y). The onset potential shifted to positive when doped with an amount of Yb smaller than y = 0.1. Above y = 0.1, the onset potential decreased with an increase in y. The mechanism of this change is discussed later.

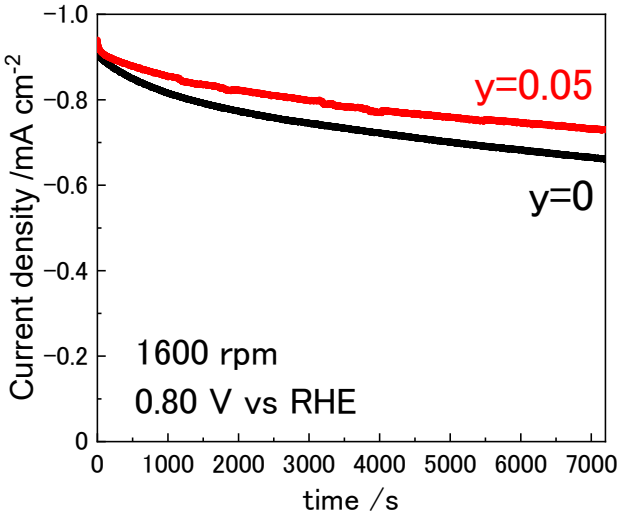

Fig. 8. Chronoamperometric curves of Yb-doped manganese nitride (y=0.05) and a non-doped manganese nitride (y=0) at 0.80 V vs RHE for 7200 s.

The stabilities of synthesized nitrides were evaluated by chronoamperometry (Figure 8). After 7200 seconds, both Yb-doped and non-doped manganese nitrides showed degradation although the degradation was less significant for the Yb-doped manganese nitrides. This result suggests that Yb doping into manganese nitride not only reduce the ORR overpotential but also potential to improve the catalyst stability.

2.3 The Effect of Other Rare-earth Elements on the ORR Activity

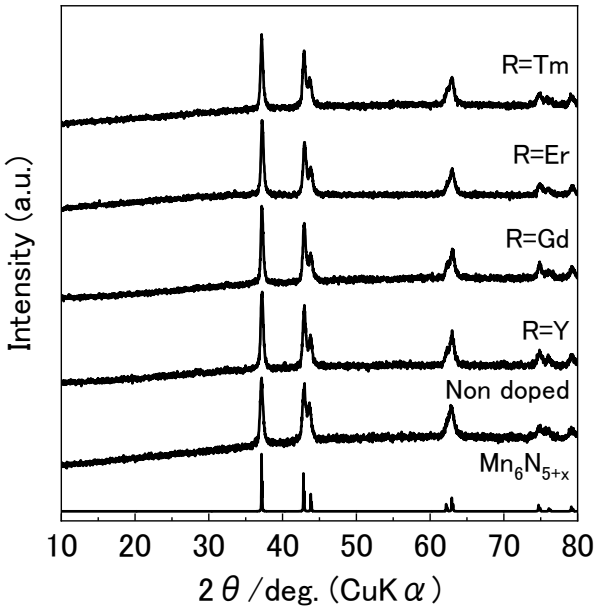

Fig. 9. XRD patterns of non-doped Mn and Mn-R-N (R=Y, Gd, Er, Tm). These samples were synthesized with a preparation ratio of R/Mn=0.01.

Table 2. Lattice constants and volumes of rare-earth (Y, Gd, Er, Tm) doped manganese nitrides acquired from the position of XRD peaks.

Doping elements	*a* /Å	*c* /Å	*V*/Å^3
Non doped	4.2051(6)	4.1412(6)	73.23(2)
Y	4.210(6)	4.131(6)	73.22(2)
Gd	4.209(7)	4.126(6)	73.09(2)
Er	4.207(3)	4.134(3)	73.17(1)
Tm	4.210(3)	4.136(8)	73.31(2)
Yb	4.2187(8)	4.1436(9)	73.75(3)

Table 3. Quantitative values of rare-earth elements contained in Mn-R-N (R=Y, Gd, Er, Tm) by ICP and EDX.

Elements	ICP (R/Mn)	EDX (R/Mn)
Y	0.028	0.028(8)
Gd	0.015	0.0048(14)
Er	0.018	0.0083(21)
Tm	0.006	0.0093(10)

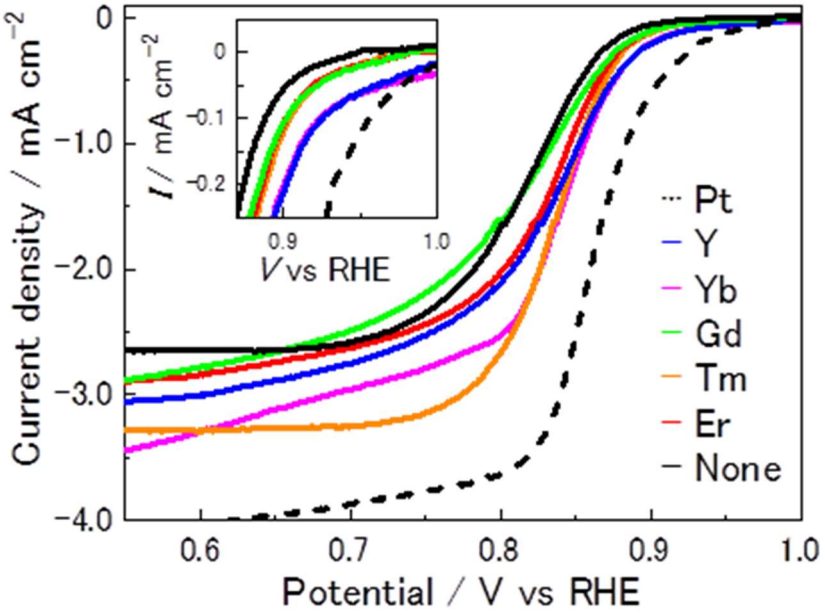

Fig. 10. LSV polarization curves of rare-earth-doped manganese nitrides (R=Y, Gd, Er, Tm, Yb). The inserted figure is an enlarged view near the onset potential.

Manganese nitrides doped with other rare-earth elements (R=Y, Gd, Er, Tm) were also synthesized through a similar process but using different rare-earth chlorides. According to the

enhanced catalytic activity of small amounts of Yb, we hypothesized that a small amount of doping of other f-block metals and Y would improve the ORR catalytic activity. All of the diffraction peaks of XRD are summarized in Fig. 9, and the diffraction peaks of XRD were indexed as Mn_6N_{5+x}[42]. Table 3 shows the lattice constants and volumes obtained from XRD patterns. Unexpectedly, some samples showed low lattice volumes. This may be caused by nonstoichiometric nature of Mn_6N_{5+x}, that needs to be further investigated. The ICP and EDX quantification results are summarized in Table 2. The ICP and EDX results showed that the products contained each rare-earth element even those amounts were close to the nominal composition (R/Mn=0.01). Small differences from the nominal composition can be caused by inhomogeneous and the error of EDX. As shown in Fig. 10, all five rare-earth-doped manganese nitrides showed higher onset potential for ORR activity than that of non-doped manganese nitrides.

3. Discussion

The self-combustion reaction is a synthetic method involving rapid heating and cooling, and it can be used to synthesize metal nitrides of various compositions[52]. The driving force of this reaction is the formation of the stable by-product NaCl from the ion exchange between sodium amide and the metal chloride[31,39]. In this paper, we emphasized that manganese nitrides doped with rare-earth elements were synthesized for the first time. We believe that the combustion reaction with rare-earth chlorides expands new nitrides containing rare-earth elements, even though the synthesis of homogeneous products remains a challenge.

Substitution of rare-earth elements into Mn sites in manganese nitrides is supported by the expansion of lattice parameters by adding Yb to the starting materials (Fig. 1(b-d)), detection of both Mn and Yb in the same area (Figs. 2 and 3), and a change in the magnetic properties (Fig. 6). The expansion of the lattice parameters can be attributed to the substitution of Yb (Yb^{3+}:0.868 Å, 6-coordinate), which has a large ionic radius of Mn^{3+} (Mn^{3+}:0.58–0.645 Å[53]), resulting in a larger lattice volume. We suppose that thermodynamically stable solid solutions composed of ions with very different radii such as Yb^{3+} and Mn^{3+} are unlikely to form. However, nitrides are the class that exceptionally produce metastable phases presumably because of their covalent nature[54]. Additionally, because the self-combustion synthesis used in this study involves rapid heating and cooling[39], it is possible to synthesize thermodynamically metastable metal nitride solid solutions such as $Mn_xMo_{1-x}N_{0.5}$[31]. Therefore, we believe that the self-combustion synthesis method enables the synthesis of metastable nitrides with rock-salt structures even though the ionic radii of composed cations are largely different.

Here, the lattice volume of pure phase in this study (73.23(3) $Å^3$) is smaller than that of the Mn_6N_{5+x} (73.501(3) $Å^3$)[42]. Because Mn_6N_{5+x} is a non-stoichiometric compound, the lattice parameters depend on nitrogen content[20]. In the XAFS measurement (Fig. 5), however, Yb doping

did not shift the absorption edge of Mn K edge. Therefore, Yb doping should have little effect on the nitrogen content. We note that there were deviations from the linear relationship between y and the lattice parameters. This may be attributed to inhomogeneity in the products synthesized by combustion reaction. In addition, the change in the magnetic moment also supports the incorporation of rare earth because this change cannot be explained by the sum of each manganese nitride and other rare-earth components.

The enhanced catalytic activity is understood by the high affinity of Yb^{3+} toward OH^-. Even though the particle size of the y=0.05 sample was comparable with y=0 and 0.1 (Fig. 3), it showed higher onset potentials. This indicates that the presence of Yb in the Mn-N lattice accelerated the ORR. The XPS O 1s spectra (Fig. 4(d)) showed a pronounced peak attributed to OH^-in the surface due to Yb doping. The ratio of the M-OH bond signal on the nitride surface increased by introducing Yb, which has a high affinity for hydroxide ions. It is considered that the promotion of the OH^- surface regeneration during the ORR process contributed to the improvement of ORR activity. The decrease in ORR activity with increasing Yb content can be attributed to the rate-limiting of hydroxide ion desorption during the ORR process due to the expansion of the hydroxide layer on the surface, or to the decrease in conductivity. Although the valence of Mn is strongly affected the catalytic activity of ORR[20,37,55], the possibility that the change in the valence of Mn from Yb doping improves catalytic activity was unlikely, as there was little change in the XPS and XANES of Mn (Figs. 4 and 5).

Finally, the enhanced catalytic activity is likely attributed to the doping of f-block elements but not to their f electron. As shown in Fig. 10, manganese nitride doped with rare-earth elements other than Yb (Y, Gd, Er, Tm) also showed higher onset potential for ORR activity than that of non-doped manganese nitrides. Because there are no f electrons in Y, the improved catalytic activity of other manganese nitrides with f-block elements is not dominantly affected by f

electrons.

4. Conclusion

A general approach to synthesizing manganese nitrides with rare-earth elements was proposed, and their enhanced catalytic activity in the ORR reaction was discovered. The novel ytterbium manganese nitrides were synthesized via self-combustion reaction using metal chlorides and sodium amide. The manganese nitrides crystallized in a tetragonal rock-salt structure, and their lattice parameters were expanded by increasing the amount of ytterbium. Interestingly, the addition of a small amount of ytterbium enhanced the ORR activity in an alkaline aqueous solution. This enhancement of catalytic activities was also confirmed by the activities of the manganese nitrides with other rare-earth metals. Since the signal of OH^- by XPS analysis became stronger after introducing an amount of ytterbium, we proposed that tuning the OH^- affinity on the surface of nitrides was a critical parameter for ORR activity.

Acknowledgement

S.H. and A.M thank Mr. Ichiro Yamane and Prof. Takashi Endo for the fruitful discussion. This research was partially supported through JSPS KAKENHI Grant Number 21H02022 and EIG CONCERT-Japan under the Strategic International Collaborative Research Program (SICORP) by Japan Science and Technology Agency (JST) (Grant Number JPMJSC17C3).

EIG CONCERT-Japan 4th Call under the Strategic International Collaborative Research Program (SICORP) of the Japan Science and Technology Agency (JST).

5. References

1 F. Wang, J. D. Harindintwali, Z. Yuan, M. Wang, F. Wang, S. Li, Z. Yin, L. Huang, Y. Fu, L. Li, S. X. Chang, L. Zhang, J. Rinklebe, Z. Yuan, Q. Zhu, L. Xiang, D. C. W. Tsang, L. Xu, X. Jiang, J. Liu, N. Wei, M. Kästner, Y. Zou, Y. S. Ok, J. Shen, D. Peng, W. Zhang, D. Barceló, Y. Zhou, Z. Bai, B. Li, B. Zhang, K. Wei, H. Cao, Z. Tan, L. bin Zhao, X. He, J. Zheng, N. Bolan, X. Liu, C. Huang, S. Dietmann, M. Luo, N. Sun, J. Gong, Y. Gong, F. Brahushi, T. Zhang, C. Xiao, X. Li, W. Chen, N. Jiao, J. Lehmann, Y. G. Zhu, H. Jin, A. Schäffer, J. M. Tiedje and J. M. Chen, *Innov.*, 2021, **2**, 100180.

2 L. Chen, G. Msigwa, M. Yang, A. I. Osman, S. Fawzy, D. W. Rooney and P. S. Yap, *Environmental Chemistry Letters*, 2022, **20**, 2277-2310.

3 European Commission-Press Release, 2020, 8–10.

4 M. K. Debe, *Nature*, 2012, **486**, 43–51.

5 M. W. Ellis, M. R. Von Spakovsky and D. J. Nelson, *Proc. IEEE*, 2001, **89**, 1808–1817.

6 W. Chen, J. Huang, J. Wei, D. Zhou, J. Cai, Z. Da He and Y. X. Chen, *Electrochem. commun.*, 2018, **96**, 71–76.

7 J. K. Nørskov, J. Rossmeisl, A. Logadottir, L. Lindqvist, J. R. Kitchin, T. Bligaard and H. Jónsson, *J. Phys. Chem. B*, 2004, **108**, 17886–17892.

8 X. Ren, Y. Wang, A. Liu, Z. Zhang, Q. Lv and B. Liu, *J. Mater. Chem. A*, 2020, **8**, 24284–24306.

9 N. Markovic, H. Gasteiger and P. N. Ross, *J. Electrochem. Soc.*, 1997, **144**, 1591–1597.

10 X. Ren, Q. Lv, L. Liu, B. Liu, Y. Wang, A. Liu and G. Wu, *Sustain. Energy Fuels*, 2019, **4**, 15–30.

11 Y. Bing, H. Liu, L. Zhang, D. Ghosh and J. Zhang, *Chem. Soc. Rev.*, 2010, **39**, 2184–2202.

12 C. Wang, N. M. Markovic and V. R. Stamenkovic, *ACS Catal.*, 2012, **2**, 891–898.

13 A. Miura, H. Wang, B. M. Leonard, H. D. Abruña and F. J. DiSalvo, *Chem. Mater.*, 2009, **21**,

2661–2667.

14 D. Wang, Y. Yu, H. L. Xin, R. Hovden, P. Ercius, J. A. Mundy, H. Chen, J. H. Richard, D. A. Muller, F. J. Disalvo and H. D. Abruña, *Nano Lett.*, 2012, **12**, 5230–5238.

15 X. Y. Lang, G. F. Han, B. B. Xiao, L. Gu, Z. Z. Yang, Z. Wen, Y. F. Zhu, M. Zhao, J. C. Li and Q. Jiang, *Adv. Funct. Mater.*, 2015, **25**, 230–237.

16 A. Miura, M. E. Tague, J. M. Gregoire, X. D. Wen, R. B. Van Dover, H. D. Abruña and F. J. Disalvo, *Chem. Mater.*, 2010, **22**, 3451–3456.

17 C. R. Raj, A. Samanta, S. H. Noh, S. Mondal, T. Okajima and T. Ohsaka, *J. Mater. Chem. A*, 2016, **4**, 11156–11178.

18 J. Xie and Y. Xie, *Chem. Eur. J.*, 2016, **22**, 3588–3598.

19 R. Zeng, Y. Yang, X. Feng, H. Li, L. M. Gibbs, F. J. DiSalvo and H. D. Abruña, *Sci. Adv.*, 2022, **8**, 1–12.

20 A. Miura, C. Rosero-Navarro, Y. Masubuchi, M. Higuchi, S. Kikkawa and K. Tadanaga, *Angew. Chemie*, 2016, **128**, 8095–8099.

21 E. Davari and D. G. Ivey, *J. Appl. Electrochem.*, 2017, **47**, 815–827.

22 M. Azuma, M. Kashihara, Y. Nakatoa and H. Tsubomura, *J. Electroanal. Chem.*, 1988, **250**, 73–82.

23 Y. Yang, R. Zeng, Y. Xiong, F. J. Disalvo and H. D. Abruña, *J. Am. Chem. Soc.*, 2019, **141**, 19241–19245.

24 M. E. Kreider, A. Gallo, S. Back, Y. Liu, S. Siahrostami, D. Nordlund, R. Sinclair, J. K. Nørskov, L. A. King and T. F. Jaramillo, *ACS Appl. Mater. Interfaces*, 2019, **11**, 26863–26871.

25 Y. Yuan, J. Wang, S. Adimi, H. Shen, T. Thomas, R. Ma, J. P. Attfield and M. Yang, *Nat. Mater.*, 2020, **19(3)**, 282-286.

26 B. Cao, J. C. Neuefeind, R. R. Adzic and P. G. Khalifah, *Inorg. Chem.*, 2015, **54**, 2128–2136.

27 B. He, Y. Yuan, J. Wang, E. Pervaiz, X. Dong, Z. Shao and M. Yang, *Electrocatalysis*, 2018, **9**, 452–458.

28 D. D. Vaughn, J. Araujo, P. Meduri, J. F. Callejas, M. A. Hickner and R. E. Schaak, *Chem. Mater.*, 2014, **26**, 6226–6232.

29 K. E. Fritz, Y. Yan and J. Suntivich, *Nano Res.*, 2019, **12**, 2307–2312.

30 J. Luo, X. Tian, J. Zeng, Y. Li, H. Song and S. Liao, *ACS Catal.*, 2016, **6**, 6165–6174.

31 J. Odahara, W. Sun, A. Miura, N. C. Rosero-Navarro, M. Nagao, I. Tanaka, G. Ceder and K. Tadanaga, *ACS Mater. Lett.*, 2019, **1**, 64–70.

32 R. Niewa, G. V. Vajenine, F. J. DiSalvo, H. Luo and W. B. Yelon, *Zeitschrift für Naturforsch. B,* 1998, **53**, 63–74.

33 K. R. Talley, C. L. Perkins, D. R. Diercks, G. L. Brennecka and A. Zakutayev, *Science,* 2021, **1491**, 1488–1491.

34 S. D. Kloß, M. L. Weidemann and J. P. Attfield, *Angew. Chemie*, 2021, **60**, 22260–22264.

35 I. I. Diakonov, K. V. Ragnarsdottir and B. R. Tegirov, *Chem. Geol.*, 1998, **151**, 327–347.

36 J. T. Mefford, X. Rong, A. M. Abakumov, W. G. Hardin, S. Dai, A. M. Kolpak, K. P. Johnston and K. J. Stevenson, *Nat. Commun.*, 2016, **7**, 11053.

37 J. Suntivich, H. A. Gasteiger, N. Yabuuchi, H. Nakanishi, J. B. Goodenough and Y. Shao-Horn, *Nat. Chem.*, 2011, **3**, 546–550.

38 A. Miura, T. Takei and N. Kumada, *Inorg. Chem.*, 2013, **52**, 11787–11791.

39 S. Noguchi, J. Odahara, H. Sakai, N. C. Rosero-Navarro, A. Miura and K. Tadanaga, *Inorg. Chem.*, 2021, **60**, 12753–12758.

40 J. Odahara, A. Miura, N. C. Rosero-Navarro and K. Tadanaga, *Inorg. Chem.*, 2018, **57**, 24–27.

41 L. Chen, Y. Gu, L. Shi, Z. Yang, J. Ma and Y. Qian, *Solid State Commun.*, 2004, **132**, 343–346.

42 A. Leineweber, R. Niewa, H. Jacobs and W. Kockelmann, *J. Mater. Chem.*, 2000, **10**, 2827–

2834.

43 R. Sheikholeslami and J. Bright, *Desalination*, 2002, **143**, 255–267.

44 D. Briggs and N. Fairley, *Surf. Interface Anal.*, 2002, **33**, 274–282.

45 M. Oku, K. Hirokawa and S. Ikeda, *J. Electron Spectros. Relat. Phenomena*, 1975, **7**, 465–473.

46 E. McCafferty and J. P. Wightman, *Surf. Interface Anal.*, 1998, **26**, 549–564.

47 D. Jaeger and J. Patscheider, *J. Electron Spectros. Relat. Phenomena*, 2012, **185**, 523–534.

48 Y. Ohno, *J. Electron Spectros. Relat. Phenomena*, 2008, **165**, 1–4.

49 S. Civiš, A. Knížek, P. B. Rimmer, M. Ferus, P. Kubelík, M. Zukalová, L. Kavan and E. Chatzitheodoridis, *ACS Earth Sp. Chem.*, 2019, **3**, 221–232.

50 Y. Zhao, C. Xie, Y. Song and P. Yang, *J. Nanoparticle Res.*, 2020, **22**, 147.

51 R. C. Rai, C. Horvatits, D. McKenna and J. Du Hart, *AIP Adv.*, 2019, **9**, 015019.

52 E. G. Gillan and R. B. Kaner, *Chem. Mater.*, 1996, **8**, 333–343.

53 R. D. Shannon, *Acta Cryst.*, 1976, **A32**, 751.

54 W. Sun, S. T. Dacek, S. P. Ong, G. Hautier, A. Jain, W. D. Richards, A. C. Gamst, K. A. Persson and G. Ceder, *Sci. Adv.*, 2016, **2(11)**, e1600225.

55 Y. Iwai, A. Miura, N. C. Rosero-Navarro, M. Higuchi and K. Tadanaga, *J. Asian Ceram. Soc.*, 2019, **7**, 147–153.